https://doi.org/10.5194/egusphere-2026-5223
Preprint. Discussion started: 9 September 2026

Global spatial and temporal variations of gravity-wave-induced heat fluxes and heating rates based on SABER's observations

Xiao Liu[1, 2], Jiyao Xu[2, 3], Jia Yue[4, 5], Qinzeng Li[2], Zhaoai Yan[2], Yangkun Liu[1], Luiz Fillip Rodrigues Vital [2, 6] and Juliano Moro[2, 7]

[1]School of Mathematics and Statistics, Henan Normal University, Xinxiang, China

[2]State Key Laboratory of Solar Activity and Space Weather, National Space Science Center, Chinese Academy of Sciences, Beijing, China

[3]University of the Chinese Academy of Science, Beijing, China

[4]NASA Goddard Space Flight Center, Greenbelt, MD, USA

[5]Physics Department, Catholic University of America, DC, USA

[6]State University of Paraíba — UEPB, Paraíba, Brazil

[7]National Institute for Space Research - INPE, Santa Maria, Brazil

Corresponding author: Jiyao Xu (xujy@nssc.ac.cn)

Key Points:

- Global gravity wave (GW)-induced heat fluxes and heating rates are derived from SABER temperature profiles using linear GW theory.
- GW-induced heat fluxes and heating rates correlate with GW amplitudes, producing downward heat fluxes and cooling background atmosphere.
- Maxima of GW-induced heat fluxes and heating rates occur at summer high latitudes, coinciding with the cold summer mesopause.

https://doi.org/10.5194/egusphere-2026-5223
Preprint. Discussion started: 9 September 2026

Abstract

Gravity waves (GWs) play an important role in balancing the energy budget of the mesosphere and lower thermosphere (MLT) by heating/cooling the background atmosphere. The global heat fluxes and heating rates generated by non-breaking GWs are derived from SABER observations during 2002−2025. The derived heat fluxes are mainly downward and cool the background atmosphere, with peaks occurring at 80–100 km. Around 35°N, the monthly mean heat flux and heating rate are ~−0.7 Kms^{-1} and ~−12 Kday^{-1}, with standard deviations of ~1.1 Kms^{-1} and ~20 Kday^{-1}, respectively. Global GW-induced heat fluxes and heating rates exhibit stronger annual and weaker semiannual oscillations, with the stronger peak in summer hemisphere. Moreover, these quantities show notable interhemispheric and seasonal asymmetries, with larger summer amplitudes occurring at the northern high latitudes. Such interhemispheric asymmetry agrees with the colder summer mesopause at northern high latitudes. However, the heat fluxes and heating rates derived here are ~0.3−0.5 times the values lidar observations and are ~0.5 times the theoretical values and breaking GWs. These underestimations are induced by the uncertainties of GW propagation directions, observational filter, and limited GW wavelengths observable by SABER.

https://doi.org/10.5194/egusphere-2026-5223
Preprint. Discussion started: 9 September 2026

1 Introduction

In the mesosphere and lower thermosphere (MLT), the energy budget is governed by multiple coupled dynamical-chemical processes, such as solar radiative heating, photochemical heating, radiative cooling, eddy and molecular diffusivity heating, and adiabatic heating/cooling (Holton, 1983; Smith, 2004). Among the multiple processes, adiabatic heating/cooling is several times larger than other processes (Smith, 2004; Yue and Wang, 2025) and is driven by the residual meridional circulation, which is caused by breaking gravity waves (GWs) in the MLT (Fritts and Alexander, 2003; Hines, 1960; Holton, 1983). The momentum and heat dissipated by breaking GWs have been studied and parameterized in global circulation models and local numerical model (Fritts, 1984; Lindzen, 1981; Liu et al., 1999; Xue et al., 2012). Another consequence of breaking GWs is their resulting body force, which generates larger-scale secondary GWs, which propagate into a wider spatial range as compared to the primary GWs (Li, Q. et al., 2022; Vadas et al., 2003; Vadas et al., 2018). Relative to breaking GWs, theoretical and recent lidar observations showed that non-breaking GWs, which have coherent structures, can propagate into a wider spatial range and influence atmospheric thermal state along their ray path (Chu et al., 2022; Gardner, 2018; Gardner and Liu, 2007; Liu, 2009; Liu, 2000, 2021; Walterscheid, 1981; Weinstock, 1983; Xu et al., 2003). This raises the question of how to quantify the net heat induced by non-breaking GWs and their effects on atmosphere.

The polarization relations for linear GWs in a compressible atmosphere demonstrate that the phase difference ($\Delta\phi_{wT}$) between vertical wind (w') and temperature (T') perturbation deviates from 90° and is non-orthogonal. This phase difference depends on the vertical wavenumber (m), intrinsic wave frequency ($\hat{\omega}$) of GW, as well as the statistic stability of the atmosphere (Fritts and Alexander, 2003; Vadas, 2013). This non-orthogonal phase difference yields a non-zero heat flux ($\overline{w'T'}$), which is the average of the product ($w'T'$) over one wave period or wavelength. Then the non-zero heat flux heats or cools the background atmosphere. Note that, the polarization relations for linear GWs under Boussinesq approximation yield $\Delta\phi_{wT} = 90°$. This orthogonal phase difference yields $\overline{w'T'} = 0$ and zero heating rate. Previous simulation and lidar observations confirmed that $\Delta\phi_{wT}$ deviates from 90° by several degrees (Chu et al., 2022; Lu et al., 2017; Xu et al., 2003). In fact, an early study by Walterscheid (1981) showed that non-breaking GWs produce downward heat flux and cool the background atmosphere within their dissipation layers. Under typical MLT conditions, non-breaking GW-induced heating rates are of ~8–25 Kday^{-1}. Such magnitudes depend on the static stability and eddy diffusivity. By simulating the nonlinear

https://doi.org/10.5194/egusphere-2026-5223
Preprint. Discussion started: 9 September 2026

propagation of GWs and combining the linear GW saturation theory, Liu (2000) showed that upward-propagating saturated GWs induce heating rates about −36.4 $\mathrm{Kday^{-1}}$. These magnitudes are comparable with those of adiabatic heating/cooling induced by the residual meridional circulation in the MLT (Smith, 2004; Yue and Wang, 2025). Thus, the heat fluxes and heating rates induced by non-breaking GWs have been quantified by ground-based sodium lidar observations in the MLT over several stations. Unless otherwise specified, we discuss the heat fluxes and heating rates induced by non-breaking GWs.

Ground-based sodium lidar observations revealed that the GW-induced heat fluxes and heating rates can be negative or positive depending the upward or downward propagation of GWs. Their magnitudes varied greatly from case to case. Tao and Gardner (1995) adopted the sodium lidar at Haleakala (20.8°N, 156.3°W) and revealed upward heat flux below 93 km and downward heat flux above 93 km. This induces heating rates with a maximum value of ~264 $\mathrm{Kday^{-1}}$. Gardner and Yang (1998) analyzed a total of 65 hours of observations by sodium lidar and showed that the average heat flux was −2.29±0.43 $\mathrm{Kms^{-1}}$ and the average heating rate was −30.9±5.3 $\mathrm{Kday^{-1}}$ in the MLT. Recently, Guo and Liu (2021) analyzed 400 hours of sodium lidar observations between 2014 and 2017 at the Andes Lidar Observatory (ALO, 30.3°N, 70.7°W). They revealed significant annual cycles in heat fluxes, with negative peaks of −2.8 $\mathrm{Kms^{-1}}$ occurring in July at altitudes of 88–94 km. The corresponding heating rates peaked at −30 $\mathrm{Kday^{-1}}$ during June–August, with an annual average of −6.7 $\mathrm{Kday^{-1}}$. Li, T. et al. (2022) analyzed the sodium lidar observation at the Hefei station from 2012 to 2021. Their results showed that GW-induced heat fluxes exhibited seasonal fluctuations ranging between −1.2 $\mathrm{Kms^{-1}}$ and −2.0 $\mathrm{Kms^{-1}}$, yielding an average heating rate of −35 $\mathrm{Kday^{-1}}$. Chu et al. (2022) compared heat fluxes and their corresponding peak altitudes derived from lidar observations at five stations: SOR (35.0°N), Hefei (32.0°N), Maui (20.7°N), ALO (30.3°S), and McMurdo (77.8°S). The heat flux at McMurdo reached a peak of −3 $\mathrm{Kms^{-1}}$ at 84 km, while other stations displayed smaller flux peaks located at 88 km or higher. Errors and spectral range of GWs inhibited in observation are regarded as primary factors responsible for such discrepancies (Chu et al., 2022; Gardner and Liu, 2007; Guo and Liu, 2021; Su et al., 2008).

Nevertheless, GWs span a broad spatial and temporal spectra and depend on geographic locations and seasons, making high-resolution simulations computationally challenging (Becker and Vadas, 2018; Liu et al., 2024; Liu, H. L. et al., 2014). Sub-grid breaking GWs are always represented via GW parameterization schemes to get reasonable results (Guarino et al., 2024; Liu, 2021; Liu et al., 2018; Yiğit and Medvedev, 2009). Theory and ground-based lidar observations have illustrated the importance of non-breaking GWs and should also be quantified in global view.

https://doi.org/10.5194/egusphere-2026-5223
Preprint. Discussion started: 9 September 2026

Satellite observations provide global coverage but generally lack the capability to directly resolve vertical wind. To partially resolve the contradiction between the advantage of global coverage and the lack of vertical-wind measurements from satellite observations, we try to derive the GW-induced vertical wind, heat flux and heating rate from satellite measured temperature profile and the theory of linear GWs in a compressible atmosphere.

The purpose of this work is to derive the global GW-induced heat fluxes and heating rates. A short description of our flowchart is as follows: (1) We extract GW temperature perturbations from the temperature profiles measured by the Sounding of the Atmosphere using Broadband Emission Radiometry (SABER) instrument (Esplin et al., 2023; Russell et al., 1999). (2) Vertical wind perturbations are derived based on dispersion and polarization relations of linear GW in a compressible atmosphere (Ern et al., 2004; Fritts and Alexander, 2003; Vadas, 2013). In our previous studies, the GW-induced wind shears were derived from SABER-measured temperature profiles based on linear GW theory (Liu et al., 2020). (3) The heat flux and heating rate are calculated theoretically from the GW temperature and vertical velocity perturbations.

The remainder of this paper is organized as follows: Section 2 describes the theoretical basis and the procedure of deriving GW-induced parameters, such as temperature perturbations, vertical velocity perturbations, heat flux and heating rate. Section 3 analyzes the GW-induce parameters within the 35°N latitude band and their uncertainties. Section 4 provides global and monthly morphology of derived parameters. The uncertainties, comparison with lidar observations, and the influences of heating rate on the thermal structure in the MLT are discussed in Section 5. Conclusions are summarized in Section 6.

2 Method of deriving GW-induced heat flux and heating rate

Before introducing our methodology, we provide a brief summary of the key features of the temperature profiles measured by SABER. The SABER temperature profiles are from 15 km to 110 km and at 83°N–52°S or 52°N–83°S alternatively every about 60 days. For the Level 2A data, the precision of a single temperature profile increases from ~0.3 K at 15 km to 15 K at 110 km with a vertical resolution of 2 km (Dawkins et al., 2018; Remsberg et al., 2008). The SABER temperature is stable after resolving the issue of algorithm instability (Liu et al., 2026; Mlynczak et al., 2020; Mlynczak et al., 2022; Mlynczak et al., 2023) and is suitable to study the dynamics of middle atmosphere.

2.1 Theorical basis of deriving GW-induced vertical velocity perturbations

Atmospheric waves exhibit distinct temporal and spatial scales. This characteristic allows the

https://doi.org/10.5194/egusphere-2026-5223
Preprint. Discussion started: 9 September 2026

separation of small-scale temperature perturbations $T_{\text{res}}(z)$ by subtracting large-scale waves (e.g., tides and planetary waves) and background temperature from raw observational temperature profiles $T(z)$. Then, the GW-induced temperature perturbations $T'(z)$ can be reconstructed from $T_{\text{res}}(z)$ via bandpass filtering or spectral decomposition within a predefined vertical wavelength range (Alexander et al., 2008; Liu et al., 2017; Liu, X. et al., 2014; Wang and Alexander, 2010; Yamashita et al., 2013).

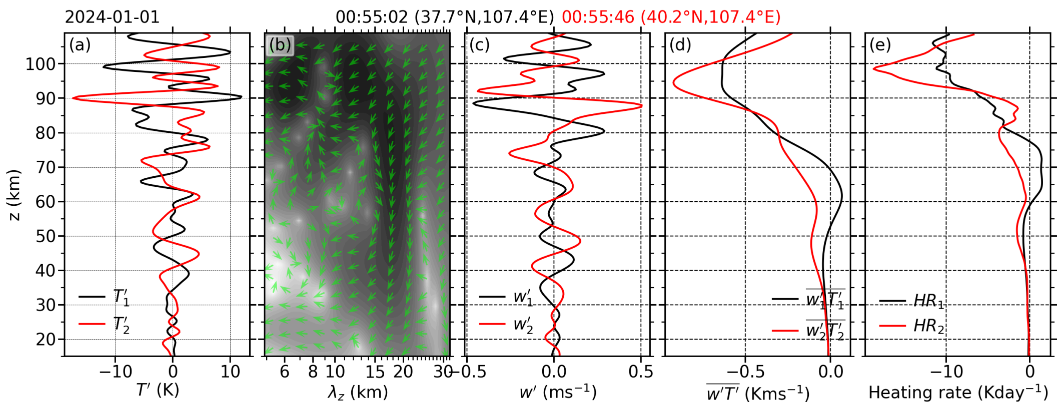

Figure 1. Procedure of deriving GW-induced parameters on 1 January 2024. (a) GW-induced temperature profiles of T_1' (black) at 37.7°N, 107.4°E and T_2' (red) at 40.2°N, 107.4°E. (b) amplitude of $W_{T_1T_2}$ in log10 scale (the magnitudes increase with the darkness), the arrow directions indicate the angles of $\Delta\phi$ (rightward for 0°, upward for 90°, leftward for 180°). (c–e): GW-induced vertical velocity, heat flux, and heating rate corresponding to T_1' and T_2', respectively.

Herein, we adopt the method detailed described in Appendix A of Liu et al. (2017) to extract $T'(z)$ from $T(z)$. A brief overview is below for completeness. First, daily SABER temperatures at ascending and descending nodes are individually selected within a 5° latitudinal band. At each node, latitudinal band and altitude, we decompose $T(z)$ into the background field $\overline{T}(z)$ and harmonic fits $T_{\text{fit}}(z)$ for zonal wavenumbers of 1–6. The residual temperature $T_{\text{res}}(z)$ is calculated as $T(z) - \overline{T}(z) - T_{\text{fit}}(z)$. Second, $T'(z)$ is reconstructed from $T_{\text{res}}(z)$ via Morlet wavelet analysis (Torrence and Compo, 1998). In this step, vertical wavelengths are constrained to 5–30 km. Figure 1(a) shows two adjacent profiles of the derived $T'(z)$ as an example.

Following a similar approach used to retrieve GW-induced wind shears (Liu et al., 2020), we derive GW-induced vertical velocity perturbations $w'(z)$ from SABER temperature observations using the dispersion and polarization relations for linear GWs. The GW-induced temperature and

https://doi.org/10.5194/egusphere-2026-5223
Preprint. Discussion started: 9 September 2026

vertical velocity perturbations are expressed as,

$$T' = A_T e^{i(\omega t - kx - mz - \phi_T)} \tag{1a}$$

$$w' = A_w e^{i(\omega t - kx - mz - \phi_w)} \tag{1b}$$

Here, $i = \sqrt{-1}$ denotes the imaginary unit. A_T and A_w are wave amplitudes, and ϕ_T and ϕ_w are wave phases. The parameters ω, k, and m correspond to the ground-based frequency, horizontal, and vertical wavenumbers, respectively.

For a compressible, f-plane, and non-dissipative atmosphere, the polarization relation linking w' and T' is written as (Chu et al., 2022; Vadas, 2013),

$$A_w = \mathcal{P}(\widehat{\omega}, m)\frac{A_T}{\overline{T}} \tag{2a}$$

$$\mathcal{P}(\widehat{\omega}, m) = \frac{-ig\widehat{\omega}}{N^2}\left[1 - \frac{i}{mH}\left(\frac{1}{2} - \frac{1}{\gamma}\right)\right] \Big/ \left[1 + \frac{i}{mH}\left(\frac{1}{2} - \frac{\gamma - 1}{\gamma}\frac{\widehat{\omega}^2}{N^2}\right)\right] \tag{2b}$$

In this equation, $\mathcal{P}(\widehat{\omega}, m)$ is the polarization coefficient. g is the gravitational acceleration, N the buoyancy frequency, and H the atmospheric scale height. The parameter γ is the specific heat ratio of dry air. The intrinsic frequency satisfies:

$$\widehat{\omega}^2 = \frac{k^2 N^2 + f^2(m^2 + 1/4H^2)}{k^2 + m^2 + 1/4H^2} \tag{3}$$

The horizontal wavenumber is calculated from the phase difference $\Delta\phi$ between two adjacent profiles separated by a horizontal distance of Δx (Alexander et al., 2008; Ern et al., 2004),

$$k = k_a = \Delta\phi / \Delta x \tag{4}$$

Note that the horizontal wavenumber k_a derived from Equation (4) is in the along-track direction. The true horizontal wavenumber k_h is therefore given by $k_h = k_a / \cos\alpha$, where α is the angle between the along-track direction and the GW propagation direction. Such that k_h increase as α increases. For instance, if $\alpha = 60°$, $k_h = 2k_a$, the true intrinsic frequency $\widehat{\omega}_h$ is approximately $2\widehat{\omega}_a$, here $\widehat{\omega}_a$ is the intrinsic frequency calculated from Equations (3) and (4). The uncertainties of α induce uncertainties in the retrieval of w', as well as the resultant heat flux and heating rate. This will be discussed in the next subsection.

2.2 GW-induced vertical velocity perturbations, heat fluxes, and heating rate

We derive the $w'(z)$ from $T'(z)$ based on the aforementioned theory and Morlet wavelet analysis (Torrence and Compo, 1998). The wavelet transform of $T'(z)$ takes the form:

$$W_T(a, z) = \frac{1}{\sqrt{a}}\int_{-\infty}^{\infty} T'(\tau)\,\psi^*\left(\frac{\tau - z}{a}\right) d\tau \tag{5a}$$

https://doi.org/10.5194/egusphere-2026-5223
Preprint. Discussion started: 9 September 2026

with the Morlet mother wavelet of

$$\psi(z) = \pi^{-1/4} e^{ik_0 z} e^{-z^2/2} \tag{5b}$$

Here, $\psi^*(z)$ is the complex conjugate of $\psi(z)$, and k_0 is the central wavenumber. The wavelet scale a relates to the physical wavelength λ and the vertical step Δz via $a = \lambda k_0 / 2\pi\Delta z$. Using Equation (5), the wavelet coefficients $W_{T_1}(a,z)$ and $W_{T_2}(a,z)$ are calculated from $T_1'(z)$ and $T_2'(z)$, respectively. The phase difference $\Delta\phi(a,z)$ between $T_1'(z)$ and $T_2'(z)$ is calculated as,

$$W_{T_1T_2}(a,z) = W_{T_1}(a,z) \cdot W_{T_2}^*(a,z) \tag{6a}$$

$$\Delta\phi(a,z) = \tan^{-1}\left[W_{T_1T_2}(a,z)\right] \tag{6b}$$

Figure 2(b) show the amplitude of $W_{T_1T_2}(a,z)$ and the phase difference between $T_1'(z)$ and $T_2'(z)$. The horizontal wavenumber k_a is calculated from $\Delta\phi(a,z)$ by Equation (4). The intrinsic frequency $\widehat{\omega}_a$ is calculated by Equation (3). Substituting these parameters into Equation (2), the wavelet coefficient of $w'(z)$ is written as,

$$W_w(a,z) = \mathcal{P}\big(\widehat{\omega}(a), m(a)\big) \cdot \frac{W_T(a,z)}{\overline{T}(z)} \tag{7}$$

Finally, $w'(z)$ is reconstructed via the inverse wavelet transform of $W_w(a,z)$,

$$w'(z) = \frac{dj\sqrt{\Delta z}}{C_\delta\, \psi_0} \sum_{j=j_{\min}}^{j_{\max}} \frac{\mathrm{Re}\left[W_w(a_j,z)\right]}{\sqrt{a_j}} \tag{8}$$

Here, $C_\delta = 0.776$ is the reconstruction constant. The summation indices $j_{\min}$ and $j_{\max}$ correspond to the scale bounds $a_{\min}$ and $a_{\max}$, which are converted from the wavelength interval $[\lambda_{\min}, \lambda_{\max}]$ with $\lambda_{\min} = 5$ km and $\lambda_{\max} = 30$ km. The vertical velocity perturbation profiles derived from $T_1'(z)$ and $T_2'(z)$ are displayed in Figure 1(c).

The GW-induced heat flux $\overline{w'T'}$ is defined as the period-averaged product of $w'T'$. The real-valued GW solutions are the real parts of Equation (1):

$$T' = A_T \cos(\omega t - kx - mz - \phi_T) \tag{9a}$$

$$w' = A_w \cos(\omega t - kx - mz - \phi_w) \tag{9b}$$

Thus, at each spatial location (x,z), the period-averaged heat flux $\overline{w'T'}$ can be analytically derived by integrating the instantaneous covariance $w'T'$ over one wave period $2\pi/\omega$,

$$\overline{w'T'}(z) = \int_0^{2\pi/\omega} T'(t)w'(t)dt = \frac{1}{2} A_w A_T \cos(\Delta\phi_{wT}),\, \Delta\phi_{wT} = \phi_w - \phi_T \tag{10}$$

The wavelet coefficients of $w'(z)$ and $T'(z)$ are denoted as $W_w(a,z)$ and $W_T(a,z)$, respectively. For monochromatic harmonic waves, the scale-resolved wavelet flux can be written as,

https://doi.org/10.5194/egusphere-2026-5223
Preprint. Discussion started: 9 September 2026

$$F(a,z)=\frac{1}{2}\mathrm{Re}[W_w W_T^*]=\frac{1}{2}|W_w||W_T|\cos(\Delta\phi_{wT})=\frac{1}{2}A_w A_T\cos(\Delta\phi_{wT}) \quad (11)$$

Here, $F(a,z)$ is the period-averaged heat flux contributed by the individual wave component corresponding to wavelet scale a at altitude z. The equality between the wavelet-derived term and the analytical flux (the last "=" of Equation 11) holds due to the two properties of the Morlet wavelet transform for harmonic signal. First, the modulus of wavelet coefficients is linearly proportional to physical wave amplitudes. Second, the retrieved phase difference agrees exactly with that of the original signal. The proportionality coefficient is fully removed via wavelet normalization during reconstruction.

To obtain the altitude-dependent total heat flux from multi-scale GW components, we integrate the scale-resolved flux $F(a,z)$ over all scales. The integration is weighted by $\Delta a_k/a_k^2$ and normalized by C_ψ:

$$\overline{w'T'}(z)=\frac{1}{C_\psi}\sum_{j=j_{\min}}^{j_{\max}}\left[F(a_k,z)\cdot\frac{\Delta a_k}{a_k^2}\right] \quad (12)$$

The vertical distributions of GW-induced heat flux derived from $T_1'(z)$ and $T_2'(z)$ are shown in Figure 1(d). The results show that the GW-induced heat flux is predominantly negative with peaks around 85 km. This indicates a downward transport of heat by upward propagating GWs. The GW-induced heating rate (HR) is further calculated as (Gardner and Yang, 1998; Weinstock, 1983),

$$HR=\frac{\partial T}{\partial t}=-\frac{1}{\bar{\rho}}\frac{\partial(\bar{\rho}\overline{w'T'})}{\partial z} \quad (13)$$

Here, $\bar{\rho}$ is the background density, which is derived in the same manner as the background temperature $\bar{T}$. Figure 1(e) shows the heating rates induced by $T_1'(z)$ and $T_2'(z)$, respectively. The results show that the heating rates are mainly negative with peaks around 90 km. This feature indicates that GW-induced perturbations effectively cool the background atmosphere in this region at least in this case.

3 The retrieved parameters and uncertainty analysis

In this section, we first show GW-induced parameters around 35°N with an offset of 5° for June and December. This latitude band is well-sampled by lidar measurements. These parameters include relative temperature perturbation, vertical velocity perturbation, heat flux and heating rate. Then, the retrieved parameters are compared against lidar-derived counterparts. To quantify discrepancies between our retrievals and lidar results, we conduct theoretical analysis to assess how the influences of angle α affects the uncertainties of the GW-induced parameters.

https://doi.org/10.5194/egusphere-2026-5223
Preprint. Discussion started: 9 September 2026

3.1 Retrieved parameters at 35°N

Figure 2 shows the amplitudes of the GW-induced relative temperature ($|T'/\bar{T}|$) and vertical velocity ($|w'|$) perturbations, and the values of $\overline{w'T'}$ and CR at 35°N in June. The mean values of in December are also shown in Figures 2(a2–d2). Since the variation of $|T'/\bar{T}|$ serves as the fundamental for deriving the other parameters, we first conduct a detailed analysis of this variable. Figure 2(a1) shows that $|T'/\bar{T}|$ exhibits substantial variability across individual profiles at every altitude. Their magnitudes increase from below to about 100 km and then decrease above 100 km. The 50th percentile (P50) magnitudes of $|T'/\bar{T}|$ are generally smaller than their arithmetic mean values. This indicates that the magnitudes of $|T'/\bar{T}|$ are predominantly distributed at small magnitudes, while extremely large outliers positively skew the mean above the P50. Generally, the mean, P10, P50 and P90 profiles exhibit similar altitude variations. This indicates that the vertical variations of $|T'/\bar{T}|$ are almost homogeneous across different statistical quantiles, despite the positively skewed distribution of individual profiles.

To quantify the gradient of vertical variations of $|T'/\bar{T}|$, we fit the P90 of $|T'/\bar{T}|$ by a function of $\exp(z/2H_A)$ at four altitude ranges (i.e., 60–70 km, 70–80 km, 80–90 km, and 90–100 km). Here H_A is the corresponding scale height. A larger H_A indicates a slower increase of the P90 of $|T'/\bar{T}|$. Figure 2(a1) shows that the fitting results (black line) and the magnitudes of H_A at the four altitude ranges. The scale heights H_T, which are calculated from averaged background temperature at the four altitude ranges, are also labeled by a magenta number. We see that the magnitudes of H_A are larger than H_T by a factor of 2–12 times. Moreover, the magnitudes of H_A are largest at 80–90 km, and are larger at 70–80 km and are smallest at 60–70 km. This indicates that the GWs dissipated throughout the altitude range. While the strongest dissipation occurs at ~70–90 km, where is just below the mesopause and coincides with persistent layers of GW dissipations (Liu et al., 2022). Above 100 km, the magnitudes of $|T'/\bar{T}|$ decrease with the increasing altitude. This is because molecular viscosity and thermal diffusivity become important in dissipating GWs (Liu et al., 2013; Ortland and Alexander, 2006; Vadas and Fritts, 2005; Xu et al., 2009). Only waves with longer vertical wavelengths can propagate into a higher altitude (Liu et al., 2013; Vadas and Fritts, 2005).

Although the vertical variations of $|w'|$ in Figure 2(b) exhibit similar variations to those of $|T'/\bar{T}|$ generally, their main differences can be ascribed to: (1) The scale heights of the P90 of $|w'|$ are larger than those of $|T'/\bar{T}|$ except at 70–80 km. As shown in Equations (2) and (3), $|w'|$ is proportional to the intrinsic frequency and thus the vertical wavelength (Chu et al., 2022; Vadas,

https://doi.org/10.5194/egusphere-2026-5223
Preprint. Discussion started: 9 September 2026

2013). Compared to $|T'/\bar{T}|$, $|w'|$ is more sensitive to high-frequency GWs (Geller and Gong, 2010). Thus, a sharper dissipation of $|w'|$ with altitudes is caused by the stronger dissipation of GWs having lower frequency and shorter vertical wavelength (Vadas and Fritts, 2005). (2) The peaks of $|w'|$ are mainly around 96 km, which is lower than peaks of $|T'/\bar{T}|$, which are around 100 km. This is mainly caused by phase difference $\Delta\phi_{wT}$ between w' and $T'/\bar{T}$ as shown in Equation (2), which deviates from 90° by several degrees (Chu et al., 2022; Lu et al., 2017; Xu et al., 2003).

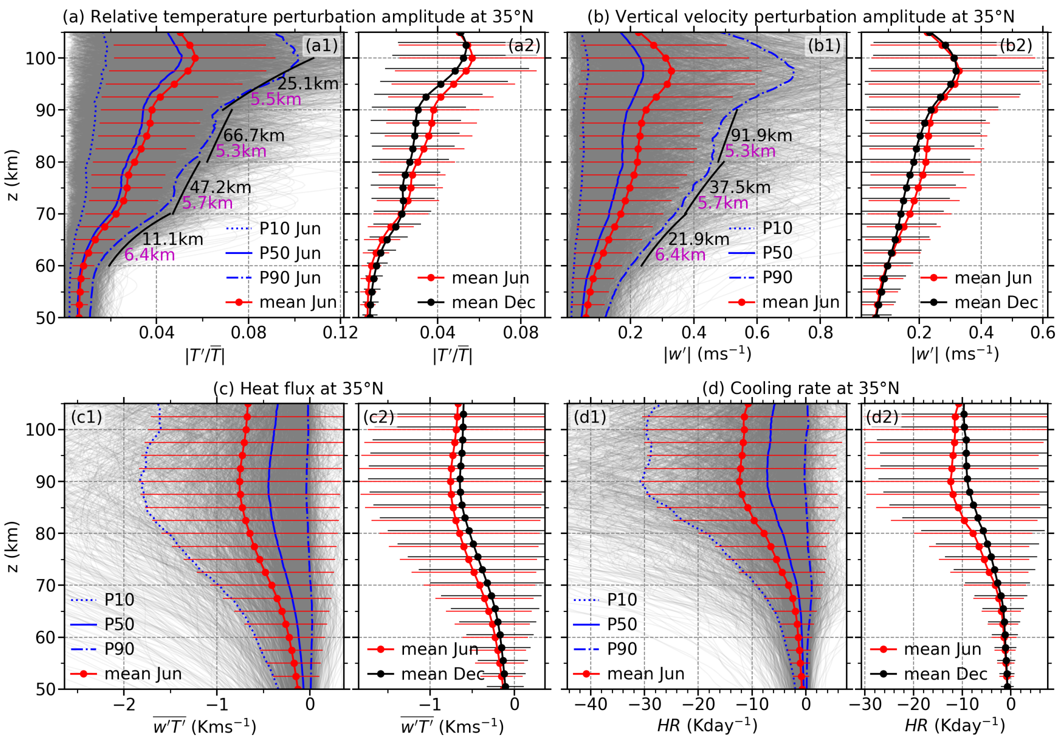

Figure 2. Overlaid profiles of the GW-induced parameters and their statistical quantiles at 35°N in June and December 2024. (a1): Profiles of $|T'/\bar{T}|$ (grey lines) and their statistics, i.e., 10th (P10: blue dot), 50th (P50: blue solid), 90th (P90: blue dash-dot) percentiles and the means (red line) and standard deviations (red error bar). (a2) The means and standard deviations of $|T'/\bar{T}|$ in June (red) and December (black). (b1–d1): same caption as (a1) but for $|w'|$, $\overline{w'T'}$, and CR, respectively. (b2–d2): same caption as (a2) but for $|w'|$, $\overline{w'T'}$, and CR, respectively.

Figures 2(c) and 2(d) show that the heat flux and heating rate exhibit large variability from one profile to another and with altitude. Their magnitudes are mainly negative, which indicates that the upward propagating GWs induce downward heat flux and cool the background atmosphere.

https://doi.org/10.5194/egusphere-2026-5223
Preprint. Discussion started: 9 September 2026

The statistical quantiles of heat flux and heating rate decrease with altitude sharply below ~90 km and then increase with altitude slowly above ~90 km. These altitude variations are different from those of $|T'/\bar{T}|$ and $|w'|$ at ~90–100 km because the heat flux and heating rate are related to both the amplitudes of $|T'/\bar{T}|$ and $|w'|$ and the phase differences between $|T'/\bar{T}|$ and $|w'|$. The heat fluxes have mean values of ~−0.7 Kms^{-1} with standard deviations of ~1.1 Kms^{-1} at 80–100 km. The heating rates have mean values of ~−12Kday^{-1} with standard deviations of ~20 Kday^{-1}. The magnitudes of P50 of heat flux and heating rate are ~0.6 times of their mean values. While the magnitudes of P90 of heat flux and heating rate are of 2.5 times of their mean values. This indicates that both heat flux and heating rate have negatively skewed distributions of individual samples. Figures 2(a2–d2) show that the absolute values of retrieved parameters are larger in June than those in December above 70 km. This indicates the seasonal variations in GW strength induce similar variations of heat flux and heating rate.

3.2 Comparison with observations and theoretical analysis

Sodium lidar can measure temperature and three-dimensional winds with high spatial and temporal resolutions. This enables the retrieval of GW-induced heat flux and heating rate. Based on 65 hours of sodium lidar observations over seven nights at Starfire Optical Range (SOR; 35°N, 107°W), Gardner and Yang (1998) derived a mean heat flux of −2.3±0.43 Kms^{-1} and a corresponding heating rate of −30.9 ±5.2 Kday^{-1}. A further analysis of 370 hours of SOR lidar observations in 1998−2000 revealed that the monthly mean heat flux exhibits semiannual variations with winter peaks of −3 Kms^{-1} and summer peaks of −1.5 Kms^{-1} around 88 km. Meanwhile, the heating rate reaches seasonal maxima of −100 Kday^{-1} in winter and −80 Kday^{-1} in summer around 90 km (Gardner and Liu, 2007). Using temperature and winds observed by a sodium lidar at Colorado State University (40.6°N, 105°W) on December 3, 2004, Li et al. (2007) investigated the heating rate associated with GW breaking. Their results indicate that the heating rate is positive between 94 and 98 km, with a maximum value of 62.4 Kday^{-1} around 96 km. Above 98 km, however, the heating rate turns negative, reaching a minimum peak of −36 Kday^{-1} near 100 km. Using 400 hours of sodium lidar observations in 2014−2017 at Andes Lidar Observatory (ALO; 30°S, 71°W), Guo and Liu (2021) showed that the heat flux is downward throughout the year below 95 km and has a peak of −3 Kms^{-1} in July. The corresponding heating rate reaches its annual peak of −30 Kday^{-1} around July. Using 400 hours of sodium lidar observations in 2012−2021 at Hefei (32°N, 117°E), Li, T. et al. (2022) showed that the heat flux varies from −1.2 Kms^{-1} to −2 Kms^{-1} throughout the year below 94 km. The annual heat flux has peak of −2 Kms^{-1}

https://doi.org/10.5194/egusphere-2026-5223
Preprint. Discussion started: 9 September 2026

at 89 km. In the 87−95 km, the mean heating rate is approximately −35 $\mathrm{Kday^{-1}}$, with a peak value of around −50 $\mathrm{Kday^{-1}}$ near 90 km. Furthermore, Chu et al. (2022) compared the heat flux and its peak altitudes based on lidar observations at five stations, including SOR (35.0°N), Hefei (32.0°N), Maui (20.7°N), ALO (30.3°S), and McMurdo (77.8°S). Their results showed that the peak heat flux at McMurdo is the strongest and reaches −3 Km $\mathrm{s^{-1}}$ at an altitude of 84 km, whereas the peaks heat fluxes at the remaining stations were smaller and occurred at altitudes of 88 km or above.

The magnitudes of the above heat flux and heating rate are mainly around their peak altitude. The heat fluxes are from −1.2 to −3 $\mathrm{Kms^{-1}}$ at altitudes ranging from 84 to 90 km. The corresponding heating rates are from −30 to −100 $\mathrm{Kday^{-1}}$ around 90 km. It should be noted that the magnitudes of heat fluxes and heating rates may be influenced by observation errors and the spatial and temporal spectral ranges of GWs resolved by observations (Gardner and Liu, 2007; Guo and Liu, 2021; Su et al., 2008). Using the linear dispersion relation for GWs and considering eddy and molecular diffusion, Weinstock (1983) derived the relation between heat flux and vertical diffusivity D_{zz},

$$\overline{w'T'} = -(H_T N^2/R) D_{zz} \tag{14a}$$

Then the heating rate is expressed as,

$$HR \approx -(N^2/R) D_{zz} \tag{14b}$$

For the typical values of $H_T = 5.5$ km, buoyancy frequency $N = 0.02\ \mathrm{s^{-1}}$, gas constant $R = 287\ \mathrm{Jkg^{-1}K^{-1}}$ and $D_{zz} = 200\ \mathrm{m^2s^{-1}}$ in the MLT, Equation (4) predicts the heat flux and heating rate are about −1.5 $\mathrm{Kms^{-1}}$ and ~−24 $\mathrm{Kday^{-1}}$. Generally, the magnitudes of heat flux and heating rate retrieved from SABER temperature measurements are ~0.3−0.5 times of those retrieved from lidar observations and are ~0.5 times of the theoretical values.

The main uncertainties of the GW-induced vertical velocity, heat flux, and heating rate arise from the undefined angle α. The true k_h and along-track k_a horizontal wavenumbers are related via $k_h = k_a/\cos\alpha$. Under the assumption of $k \ll m$, $4\pi Hm \ll 1$, and $\partial\bar{T}/\partial z \ll g/C_p$, the dispersion relation Equation (3) can be simplified as $\widehat{\omega}_h \approx N|k_h|/|m|$. This indicates that the true intrinsic frequency $\widehat{\omega}_h$ relates to $\widehat{\omega}_a$ via $\widehat{\omega}_h \approx \widehat{\omega}_a/\cos\alpha$. The module of the polarization coefficient is further simplified as $|\mathcal{P}(\widehat{\omega}_h, m)| = g\widehat{\omega}_h/N^2$ (Chu et al., 2022). This indicates that the true amplitudes A_w^h relates to the along-track amplitudes A_w^a via $A_w^h \approx A_w^a/\cos\alpha$. Based on Equation (10), the true heat flux $\overline{w'T'}_h$ relates to the along-track heat flux $\overline{w'T'}_a$ via $\overline{w'T'}_h \approx \overline{w'T'}_a/\cos\alpha$. If the angle α does not change with altitude, the true heating rate HR_h relates to the along-track heating rate HR_a via $HR_h \approx HR_a/\cos\alpha$. However, if the angle α changes altitude,

https://doi.org/10.5194/egusphere-2026-5223
Preprint. Discussion started: 9 September 2026

the term $\cos\alpha$ should be included in the vertical gradient of $\overline{w'T'}_h$. Thus, we have,

$$\frac{1}{\bar{\rho}}\frac{\partial\overline{w'T'}_h}{\partial z} = \frac{1}{\bar{\rho}}\frac{\partial(\overline{w'T'}_a/\cos\alpha)}{\partial z} = \frac{1}{\cos\alpha}\frac{1}{\bar{\rho}}\frac{\partial\overline{w'T'}_a}{\partial z} + \overline{w'T'}_a\left(\frac{\sin\alpha}{\cos^2\alpha}\right)\frac{d\alpha}{dz} \quad (15)$$

Equation (15) indicates that the altitude dependent α raises a term $\overline{w'T'}_a(\sin\alpha/\cos^2\alpha)\,d\alpha/dz$ as compared to the altitude independent α. This term complicates the estimation of uncertainties caused by α.

Generally, the uncertainties of the angle α underestimates the amplitude of the GW-induced vertical velocity and heat flux by a factor of $1/\cos\alpha$. If the angle α is independent of altitude, the derived GW-induced parameters are about $\cos\alpha$ times of the true parameters. Specifically, for $\alpha = 20°, 40°, 60°, 80°$, the values of $\cos\alpha$ are about 0.94, 0.77, 0.50, 0.17, respectively. The more complex cases are that the angle α may change from one sampling profile to another, and that the angle α may change with altitude. However, the actual propagation direction is difficult to determine by SABER limb sampling. Future tomographic limb-imaging concepts observations can retrieve atmospheric parameters across the plane perpendicular to the line of sight from each limb scan. As a candidate mission of ESA's Earth Explorer 11, the CAIRT (Changing-Atmosphere Infra-Red Tomography) is a Fourier transform infrared limb imager and observes simultaneously from the middle troposphere to the lower thermosphere with a ~400 km-wide swath. Subsequent limb-images further enable the reconstruction of three-dimensional spatial distributions of atmospheric parameters. Such capabilities will open new avenues for investigating the propagation directions and associated impacts of GWs (Errera et al., 2026; Malavart et al., 2025).

4 Global and seasonal morphology of the derived parameters

The high spatial and temporal resolutions of lidar measurements provide reliable heat flux and heating rate at ~80–100 km over several stations. Lidar observations are mainly restricted to clear-sky nighttime conditions and therefore have limited temporal continuity. However, the propagation directions of GWs cannot be retrieved from SABER observations, its continuous global observations together with the retrieval method developed in Section 2 provides an opportunity to investigate the global morphology of heat flux and heating rate. In this section, the year-to-year variations are neglected, all profiles from 2002 to 2025 are composited to form a composite year dataset. This enhances the statistical confidence of derived quantiles (e.g., the mean and P90), particularly at high latitudes.

4.1 Variations of GW amplitudes

https://doi.org/10.5194/egusphere-2026-5223
Preprint. Discussion started: 9 September 2026

Figure 3 shows the month-altitude distributions of the mean and P90 values of $|T'/\bar{T}|$ and $|w'|$ at high (75°N/S), middle (45°N/S), and low (15°N/S) latitudes. Overall, the month-altitude patterns of the mean and P90 fields of $|T'/\bar{T}|$ and $|w'|$ are qualitatively analogous. The main difference is that the magnitudes of P90 are about twice as large as their corresponding mean values. At high latitudes, both statistical quantiles exhibit altitude-dependent seasonal variations. $|T'/\bar{T}|$ is dominated by annual oscillations, with wintertime maxima in each hemisphere below ~75 km translating to summertime maxima above ~85 km. Seasonal variations are very weak at ~75–85 km transition layer. Above ~85 km, weak winter peaks emerge at 75°S, whereas no such feature is evident at 75° N. At middle latitudes, the seasonal variations are similar to those at high latitudes. The main difference is that the hemispheric winter maxima shift downward from ~75 km at high latitudes to ~70 km at middle latitudes. In addition, the semiannual oscillations at ~70–80 km are stronger than those seen at high latitudes. By comparison, the seasonal oscillations at low latitudes are far weaker than their mid- and high-latitude counterparts.

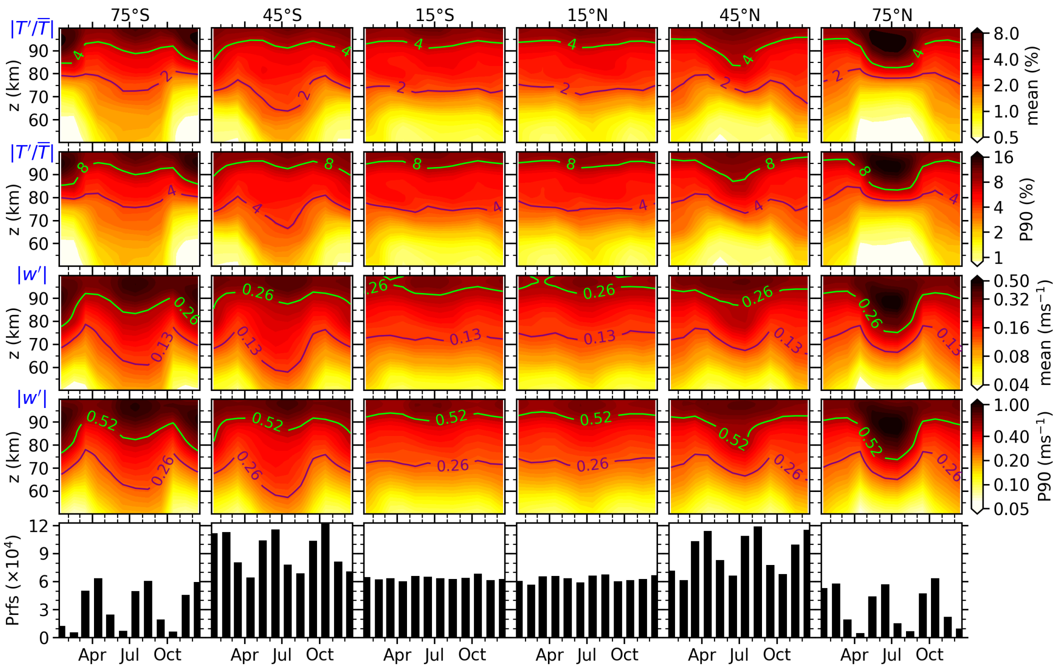

Figure 3. Month-altitude distributions of monthly-mean and monthly-P90 of $|T'/\bar{T}|$ (1st and 2nd rows) and $|w'|$ (3rd and 4th rows) at high (75°N/S), middle (45°N/S), and low (15°N/S) latitudes. Bottom row shows the numbers of profiles. Here, the month denotes the composite month derived over 2002–2025.

The mean and P90 of $|w'|$ exhibit altitude-dependent seasonal oscillations analogous to those

https://doi.org/10.5194/egusphere-2026-5223
Preprint. Discussion started: 9 September 2026

of $|T'/\bar{T}|$. Two key distinctions exist between the two fields. First, the annual maxima of $|w'|$ in each hemisphere shift downward relative to $|T'/\bar{T}|$. The annual maxima of $|w'|$ occurs near ~90 km, while the corresponding maximum of $|T'/\bar{T}|$ is located at ~ 95 km. Second, pronounced semiannual oscillations in $|w'|$ occurs at ~60–75 km and across middle and high latitudes. The semiannual oscillations have maxima in winter and summer months of each hemisphere. Notably, such summer semiannual maxima below 75 km are absent in $|T'/\bar{T}|$. A plausible physical explanation of the summum maxima of $|w'|$ below 75 km is that w' is more sensitive to the high-frequency GWs (Equation 2). In summer, convection is one of the dominant GW sources, emitting abundant high-frequency GWs with fast horizontal phase speed. These GWs can propagate upward into the stratosphere and mesosphere and thus generate the summer maxima. The seasonal variations of $|T'/\bar{T}|$ and $|w'|$ are strongest at high latitudes, stronger at middle latitudes, and weak at low latitudes. The seasonal variations vary continuously across latitude bands and can be interpreted as a genuine physical feature, rather than an artifact arising from uneven monthly sampling profiles.

The latitude-altitude distributions of the means of $|T'/\bar{T}|$ show that their maxima are at high latitudes around summer months above ~85 km (Figure 4). Specifically, in January, February, November, and December, their maxima are at latitudes higher than 50°S. In May, June, July, and August, their maxima are at latitudes higher than 50°N. Below ~75 km, the means of $|T'/\bar{T}|$ reach their maxima around 60°±20° in the winter hemisphere and weaker peaks around 20°±10° in the summer hemisphere. Moreover, the pattern suggests that the summer maxima at high latitudes above ~85 km is originates from low- and mid-latitudes (i.e., 10°–30° of the summer hemisphere) at ~50 km. The latitude-altitude distributions of the means of $|w'|$ exhibit similar pattern as those of $|T'/\bar{T}|$ in each month. The differences can be attributed to two aspects. First, the heights of summer maxima at high latitudes of $|w'|$ are ~5 km lower than those of $|T'/\bar{T}|$ in the same month. For example, in January and at latitudes higher than 50°S, the maxima of $|w'|$ and $|T'/\bar{T}|$ are at ~90 km and ~95 km, respectively. Second, the means of $|w'|$ have peaks at high latitudes of winter hemisphere above ~85 km, which are weaker and at a lower height as compared to their summer maxima.

Figures 3 and 4 reveal that winter maxima of $|w'|$ above ~85 km over the southern high latitudes exceed their northern counterparts. This indicates the pronounced hemispheric asymmetry in $|w'|$. The means of $|T'/\bar{T}|$ exhibit similar hemispheric asymmetry, though the interhemispheric contrast is less pronounced compared to that of $|w'|$. Also, above ~85 km, the

https://doi.org/10.5194/egusphere-2026-5223
Preprint. Discussion started: 9 September 2026

summer maxima of both $|T'/\bar{T}|$ and $|w'|$ at northern high latitudes are larger than their southern counterparts. Furthermore, the summer peaks of both $|T'/\bar{T}|$ and $|w'|$ are stronger than their winter counterparts over high latitudes. These features demonstrate clear interhemispheric and seasonal asymmetries in the GW amplitudes at high latitudes. However, such interhemispheric and seasonal asymmetries of the GW amplitudes are less distinct at low latitudes.

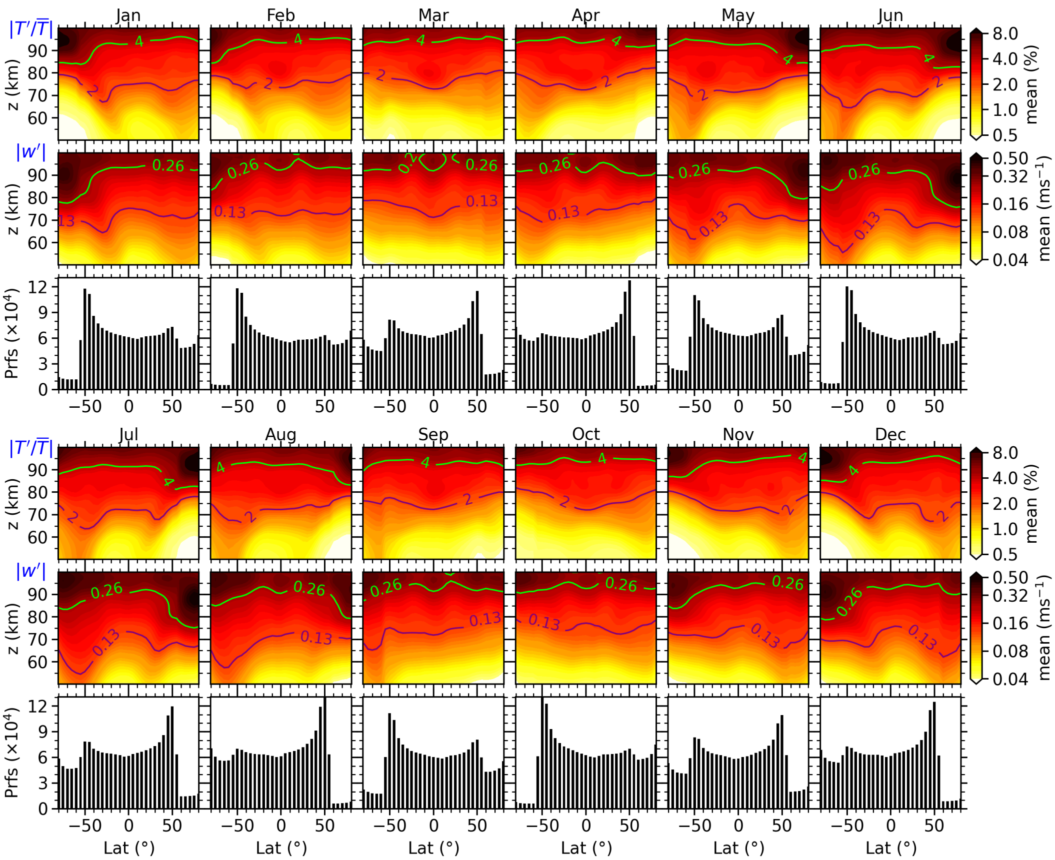

Figure 4. Latitude-altitude distributions of monthly-mean of $|T'/\bar{T}|$ (1st and 4th rows) and $|w'|$ (2nd and 4th rows) in each month. The numbers of profiles are shown in the 3rd and 6th rows.

Although the number of sampled profiles poleward of 55°S is substantially lower in January and February compared with November and December. This uneven distribution of sampling profiles at high latitudes is caused by the yaw-maneuver of SABER. However, the corresponding latitude-altitude patterns remain consistent across these four months. A minor distinction is that the latitudinal gradients of the means of $|T'/\bar{T}|$ are steeper around 55°S in January and February

https://doi.org/10.5194/egusphere-2026-5223
Preprint. Discussion started: 9 September 2026

than in November and December. Likewise, May and June exhibit latitude–altitude patterns and similarly intensified meridional gradients around 55°S as observed in July and August. These results further confirm that uneven sampling counts poleward of 55° in both hemispheres do not influence the physical characteristics governing the seasonal and latitudinal variability of $|T'/\bar{T}|$, yet they introduce sharper meridional transitions around 55°N/S.

4.2 Variations of heat flux and heating rate

Figure 5 shows the statistical quantiles (mean and P90) of heat flux ($\overline{w'T'}$) and heating rate (HR) as a function of month and altitude at six latitude bands ranging from high to low latitudes of each hemisphere. Generally, the means and P90 of heat flux exhibit similar month-altitude patterns. The magnitudes of P90 of heat flux are two times larger than the corresponding means. The means and P90 of heating rate are in a similar situation to heat flux. The P90 of heat flux and heating rate shown here is only to illustrate their large variabilities and negative skewness at each height. The following analysis focuses on the means of heat flux and heating rate.

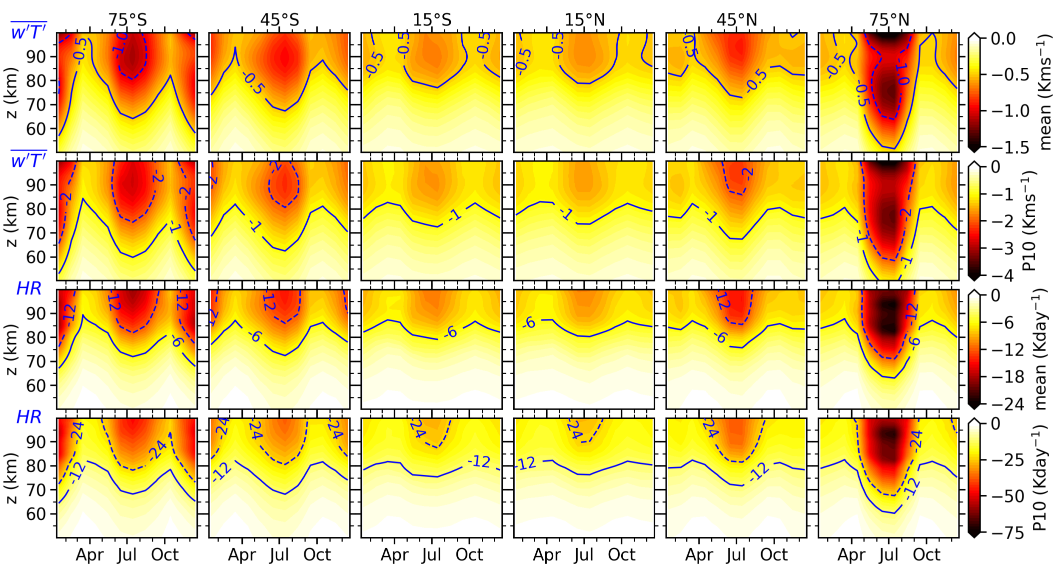

Figure 5. Month-altitude distributions of monthly-mean and montly-P90 of heat flux (1st and 2nd rows) and heating rate (3rd and 4th rows) at high (75°N/S), middle (45°N/S), and low (15°N/S) latitudes.

The heat flux in Figure 5 exhibits clear semiannual oscillation at 75°S and annual oscillation at 75°N. The peaks appear in winter and summer at 75°S and in summer at 75°N. While the peaks around December is stronger than those around July. At middle latitudes of both hemisphere, the

https://doi.org/10.5194/egusphere-2026-5223
Preprint. Discussion started: 9 September 2026

annual oscillations are superimposed by semiannual oscillations with stronger peaks around July. At low latitudes of both hemispheres, the semiannual oscillations are in the dominant position with comparable peaks in summer and winter. We note that the peak magnitudes in summer of both hemispheres increase with the increasing latitudes. These features of annual and semiannual oscillation can also be seen in heating rates. However, both heat flux and heating rate exhibit interhemispheric and seasonal asymmetries. These asymmetries can be summarized as follows. First, the summer maxima are ~−1.5 $\mathrm{Kms^{-1}}$ at 75°N, which are larger than the corresponding values of ~−1.0 $\mathrm{Kms^{-1}}$ at 75°S. The winter maxima are ~−0.8 $\mathrm{Kms^{-1}}$ at 75°N, which are less than the corresponding values of ~−1.2 $\mathrm{Kms^{-1}}$ at 75°S. Second, at 75°N, the summer maxima occur at altitudes of ~75 km and ~100 km, separated by a valley at ~88 km. This vertical valley structure is less pronounced at 75°S. We note that the vertical valley structure of summer heating rate maxima is less pronounced as compared to that of heat flux at 75°N. Third, according to the contour lines (−0.5 $\mathrm{Kms^{-1}}$ for heat flux and −12 $\mathrm{Kday^{-1}}$ for heating rate), the summer maxima extend over a wider altitude range at 75°N than at 75°S. Fourth, the heating rate at 75°S has equivalent magnitudes in summer and winter above 80 km. In contrast, the heating rate at 75°N is much larger in summer than in winter. These show the interhemispheric asymmetry in both the magnitude and vertical structure of the summer maxima of heat flux and heating rate.

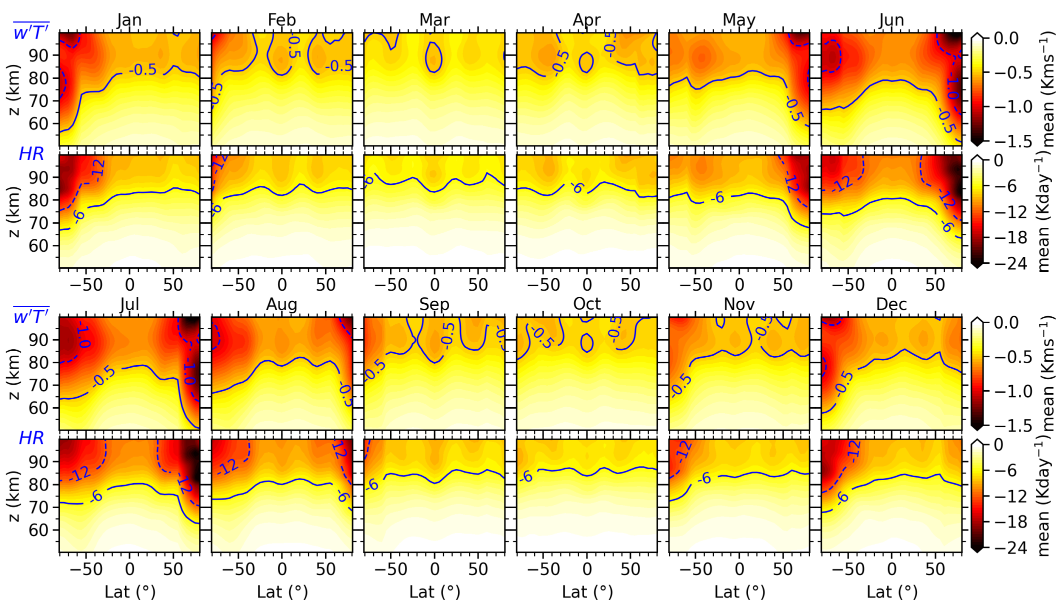

Figure 6. Latitude-altitude distributions of monthly-mean heat flux (1st and 3rd rows) and heating rate (2nd and 4th rows).

https://doi.org/10.5194/egusphere-2026-5223
Preprint. Discussion started: 9 September 2026

Figure 6 shows the latitude-altitude distributions of heat flux and heating rate to characterize their latitudinal variations in each month. During November–February, the heat flux and heating rate reach their peaks at southern high latitudes. In contrast, during May–August, the heat flux and heating rate exhibit dual peak structures at high latitudes in both hemispheres. Additionally, the substantially larger magnitudes occur at northern high latitudes. Combined with the results in Figure 5, these patterns demonstrate clear interhemispheric and seasonal asymmetries. The summer (May–August) high-latitude peaks of heat flux and heating rate in the Northern Hemisphere feature larger amplitudes. They also span a broader vertical extent. By comparison, the corresponding high-latitude peaks in the Southern Hemisphere's summer (November–February) and winter (May–August) are weaker. During equinoctial months (March, April, September, and October), weak peaks of heat flux and heating rate emerge around the equator and 50°N/S.

5 Discussion

Based on the linear GW dispersion and polarization relation in a compressible atmosphere, the global GW-induced heat flux and heating rate are derived from SABER temperature measurements. The main assumption is that the GW propagating in the along-track direction of SABER orbit. The uncertainties are quantified by introducing an angle α, which denotes the deviation of the actual GW propagating direction relative to the along-track direction. In the simple case that the angle α does not change with altitude, the retrieved heat flux and heating rate are systematically underestimated by a factor of $\cos\alpha$. Overall, the monthly mean heat flux and heating rate are of ~−0.7 Kms^{-1} and ~−12 Kday^{-1}, with standard deviations of ~1.1 Kms^{-1} and ~20 Kday^{-1}, respectively. They are ~0.3–0.5 times the lidar-derived values and are ~0.5 times of theoretical predictions.

Despite these inherent uncertainties, the GW-induced heat flux and heating rate presented in this study offer distinct advantages, including global spatial coverage and continuous temporal coverage spanning from 2002 to 2025. The heat flux and heating rate derived here are strongly correlated to the GW amplitudes, exhibiting latitudinal dependence in both annual and semiannual oscillation, as well as interhemispheric and seasonal asymmetries in their peak magnitudes. The month-altitude patterns of GW amplitudes and GW-induced heat flux and heating rate are comparable with nighttime lidar observations at SOR (35°N) reported by Gardner and Liu (2007). Their lidar results showed that GW temperature variance (T'^2) reaches its maxima in winter and summer at altitudes above 100 km and ~85−95 km, with winter peaks larger than summer ones. In

https://doi.org/10.5194/egusphere-2026-5223
Preprint. Discussion started: 9 September 2026

contrast, vertical wind variance is dominated by annual oscillations and is maximized in summer. The summer peaks occur near 85 km and 92 km, which are lower in altitude than the corresponding peaks of temperature variance. These seasonal and altitudinal features support the results presented in Figure 3. The SOR lidar-derived heat flux and heating rate exhibit negative peaks near 90 km in both winter and summer, with winter peaks being more negative than summer counterparts. Gardner and Liu (2007) suggested that variations in heat flux and heating rate are closely related to GW intensity. The GW-induced heat flux and heating rate derived here support this conclusion.

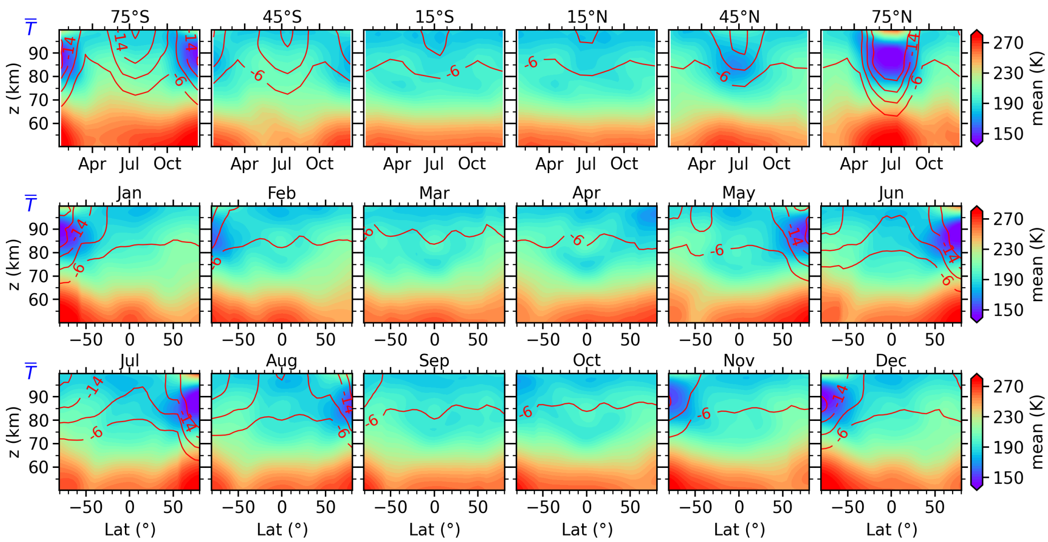

Figure 7. Monthly-mean of background temperature as a function of month and latitude (1st rows) and as a function of latitude and altitude (2nd and 3rd rows). The heating rate is overplotted by contour lines with interval of 4 Kday^{-1}.

Nevertheless, several discrepancies exist between the two results. First, unlike the lidar observations, there is no the summer maximum of T'^2 above 100 km in Figure 3. This is because of wavelet edge effects during GW extraction from SABER temperature measurements. We do not analyze GWs extracted from SABER temperature above 100 km. Second, the lidar-observed T'^2 valley near 95 km is absent in our results. T'^2 oscillates at twice the wavenumber and varies with the instantaneous phase of the perturbation. The amplitude in Equation (1) is calculated from the Hilbert transform, which removes the dependence on instantaneous phase in T'^2 and represents the slowly varying envelope of the perturbation. Third, the month-altitude patterns of lidar-derived heat flux and heating rate are more complex than those derived here. Fourth, positive values of

https://doi.org/10.5194/egusphere-2026-5223
Preprint. Discussion started: 9 September 2026

heat flux and heating rate retrieved from lidar are not fully reproduced here. The last two discrepancies are likely attributed to the distinct GW spectral ranges resolved by lidar and SABER.

Now, we discuss the relations of global morphology between heating rate and background temperature. Figure 7 shows the distributions of monthly-mean background temperature as a function of month and altitude and as a function of latitude and altitude. Comparisons between the GW-induced heating rate and background temperature show that the cold summer mesopause coincides well with the enhanced heating rates at mid- and high-latitude. Furthermore, the summer mesopause is colder at 75°N and 45°N than that at 75°S and 45°S, respectively. This feature is consistent with enhanced summer heating rates over northern mid- and high-latitude. At low latitudes, the stronger heating rate in summer is consistent with the slightly colder mesosphere relative to other seasons. The relations among GWs' strength, mesopause height and temperature at high latitudes have been studied through global models with different GW parameterization schemes and GW sources (Berger and Von Zahn, 1999; Garcia and Solomon, 1985; Siskind et al., 2003). The summer mesopause structures exhibit large discrepancies among different models. A general conclusion is that adiabatic heating/cooling caused by the meridional circulation, which is sensitive to GW forcing. This illustrates the importance of quantifying the strengths of GWs and their heating/cooling rates.

The energy balance is controlled by many dynamical and chemical processes in the MLT. The solar heating and chemical heating are ~10 K/day^{-1} and ~10−15 K/day^{-1}, respectively (Mlynczak and Solomon, 1993; Smith, 2004; Wu et al., 2026; Xu et al., 2007). Radiative cooling caused by CO_2 is about −15 K/day^{-1} (Mlynczak et al., 2024; Mlynczak et al., 2018). The adiabatic heating and cooling rates caused by meridional circulation reach peaks about 15 K/day^{-1} in the winter polar MLT and −15 K/day^{-1} in the summer polar MLT, respectively (Smith, 2004; Yue and Wang, 2025). Compared to the above-mentioned heating/cooling rates, the GW-induced heating rates are of the order of ~10 K/day^{-1}, which are in quantitative agreement with the adiabatic cooling rates. This quantitative comparison illustrates the importance of non-breaking GWs in heating/cooling the local atmosphere.

We note that the enhanced heating rates extend from about 70 km to 100 km, whereas, the heights of mesopause heights are mainly at ~85−95 km at high latitudes of summer hemispheres. This indicates that the enhanced heating rates above mesopause are not the only factor of determining the thermal structure of the lower thermosphere. In fact, the spatial and temporal variations of the thermal structures are determined by many heating/cooling sources. Specifically, although the diffusive and O_2 heating rates are very small, they increase with altitude and reach

https://doi.org/10.5194/egusphere-2026-5223
Preprint. Discussion started: 9 September 2026

peaks of ~10−20 K/day^{-1} at ~100−110 km (Smith, 2004). Moreover, the narrow warm region above the cold summer mesopause has also been revealed by Yue and Wang (2025). This may be partially explained by the decreasing adiabatic cooling rate above summer mesopause and auroral heating (Smith, 2004; Yue and Wang, 2025).

6 Conclusions

The importance of heat flux and heating rate induced by non-breaking GWs have been quantified by ground-based lidar observations. Their global distributions are unknown yet. This is due to the unavailable vertical wind measurement. To partially overcome this limitation, we derive the GW-induced vertical wind via the linear GW theory in a compressible atmosphere from the temperature profiles measured by SABER during 2002–2025. Then the global the GW-induced heat flux and heating rate are also derived. The main conclusions are summarized as below.

The GW-induced parameters ($|T'/\bar{T}|$, $|w'|$, heat flux, and heating rate) at 35°N are analyzed and compared with lidar observations. The derived heat fluxes are mainly downward and cool the background atmosphere, which peak magnitudes occurring around 90 km. The heat fluxes and heating rates have mean values of ~−0.7 Kms^{-1} and ~−12Kday^{-1}, with standard deviations of ~1.1 Kms^{-1} and ~20 Kday^{-1} at 80–100 km, respectively. The derived heating rates are almost equivalent to the adiabatic cooling rates reported before.

The global spatial and temporal distributions of the GW-induced parameters are studied in a composite year derived over 2002–2025. The annual oscillations are dominant in $|T'/\bar{T}|$ and $|w'|$ at high latitudes of summer hemispheres. The annual maxima of $|T'/\bar{T}|$ and $|w'|$ are located at ~ 95 km and ~90 km, respectively. In contrast, heat fluxes and heating rates exhibit clear semiannual oscillations, with peaks in both winter and summer hemispheres. Moreover, GW-induced parameters show notable interhemispheric and seasonal asymmetries, especially at high latitudes. Such interhemispheric asymmetry supports the colder summer mesopause at northern high latitudes as compared to that at southern high latitudes.

The magnitudes of heat fluxes and heating rates are ~0.3−0.5 times the lidar-derived values and are ~0.5 times of the theoretical values. This discrepancy is mainly attributed to uncertainties of wave propagation direction. The uncertainty of GW propagation direction underestimates heat fluxes and heating rates by a factor of $\cos\alpha$. Moreover, the observational filter and wavelengths observable by SABER are favor waves with long horizontal wavelengths. Thus, the unobserved waves with short wavelengths, which can also contribute to heat fluxes and heating, are omitted and induce an underestimation. Future tomographic limb-imaging observations (e.g., CAIRT) and high resolution model simulations, can provide three-dimensional atmospheric parameters and overcome these limitations.

Data availability

All SABER data can be accessed from Space Physics Data Facility, Goddard Space Flight Center (https://spdf.gsfc.nasa.gov/pub/data/timed/saber/, last access: March 2026). Outputs of the method are available from the corresponding author upon request.

Author contributions

XL developed the conceptualization, formal analysis and drafted the manuscript. JX and JY provided supervision, discussion and validation. QL, ZY, YL, LV, and JM provided suggestions and revisions and helpful discussion.

Competing interests

The authors declare that they have no conflict of interest.

Acknowledgments

This work was supported by the National Natural Science Foundation of China (42574216, 42404170), the Project of Stable Support for Youth Team in Basic Research Field of Chinese Academy of Sciences (grant no. YSBR-018), This work was also supported by the Specialized Research Fund for State Key Laboratory of Solar Activity and Space Weather. JM thanks the Brazilian Ministry of Science, Technology and Innovation (MCTI), National Council for Scientific and Technological Development (CNPq) Grant 305041/2024-0.

References

Alexander, M. J., Gille, J., Cavanaugh, C., Coffey, M., Craig, C., Eden, T., Francis, G., Halvorson, C., Hannigan, J., Khosravi, R., Kinnison, D., Lee, H., Massie, S., Nardi, B., Barnett, J., Hepplewhite, C., Lambert, A., and Dean, V.: Global estimates of gravity wave momentum flux from High Resolution Dynamics Limb Sounder observations, Journal of Geophysical Research: Atmospheres, 113, 10.1029/2007jd008807, 2008.

Becker, E. and Vadas, S. L.: Secondary gravity waves in the winter mesosphere: results from a high-resolution global circulation model, Journal of Geophysical Research: Atmospheres, 123, 2605–2627, 10.1002/2017jd027460, 2018.

Berger, U. and von Zahn, U.: The two-level structure of the mesopause: A model study, Journal of Geophysical Research: Atmospheres, 104, 22083–22093, 10.1029/1999jd900389, 1999.

Chu, X., Gardner, C. S., Li, X., and Lin, C. Y. T.: Vertical transport of sensible heat and meteoric Na by the complete temporal spectrum of gravity waves in the MLT above McMurdo (77.84°S, 166.67°E), Antarctica, Journal of Geophysical Research: Atmospheres, 127, 10.1029/2021jd035728, 2022.

Dawkins, E. C. M., Feofilov, A., Rezac, L., Kutepov, A. A., Janches, D., Höffner, J., Chu, X., Lu, X., Mlynczak, M. G., and Russell, J.: Validation of SABER v2.0 operational temperature data with

https://doi.org/10.5194/egusphere-2026-5223
Preprint. Discussion started: 9 September 2026

ground-based lidars in the mesosphere-lower thermosphere region (75–105 km), Journal of Geophysical Research: Atmospheres, 123, 9916–9934, 10.1029/2018jd028742, 2018.

Ern, M., Preusse, P., Alexander, M. J., and Warner, C. D.: Absolute values of gravity wave momentum flux derived from satellite data, Journal of Geophysical Research: Atmospheres, 109, 10.1029/2004jd004752, 2004.

Errera, Q., Op de beeck, M., Bender, S., Flemming, J., Funke, B., Hoffmann, A., Höpfner, M., Livesey, N., Poli, G., Pieroux, D., Raspollini, P., and Sinnhuber, B.-M.: On the capability of the Changing Atmosphere Infra-Red Tomography explorer (CAIRT) candidate mission to constrain O3 and H2O in the upper troposphere and lower stratosphere, Atmospheric Measurement Techniques, 19, 2601–2620, 10.5194/amt-19-2601-2026, 2026.

Esplin, R., Mlynczak, M. G., Russell, J., and Gordley, L.: Sounding of the Atmosphere Using Broadband Emission Radiometry (SABER): instrument and science measurement description, Earth and Space Science, 10, 10.1029/2023ea002999, 2023.

Fritts, D. C.: Gravity wave saturation in the middle atmosphere: A review of theory and observations, Reviews of Geophysics, 22, 275–308, 1984.

Fritts, D. C. and Alexander, M. J.: Gravity wave dynamics and effects in the middle atmosphere, Reviews of Geophysics, 41, 10.1029/2001rg000106, 2003.

Garcia, R. R. and Solomon, S.: The effect of breaking gravity waves on the dynamics and chemical composition of the mesosphere and lower thermosphere, Journal of Geophysical Research: Atmospheres, 90, 3850–3868, 10.1029/JD090iD02p03850, 1985.

Gardner, C. S.: Role of wave-induced diffusion and energy flux in the vertical transport of atmospheric constituents in the mesopause region, Journal of Geophysical Research: Atmospheres, 123, 6581–6604, 10.1029/2018jd028359, 2018.

Gardner, C. S. and Liu, A. Z.: Seasonal variations of the vertical fluxes of heat and horizontal momentum in the mesopause region at Starfire Optical Range, New Mexico, Journal of Geophysical Research: Atmospheres, 112, 10.1029/2005jd006179, 2007.

Gardner, C. S. and Yang, W.: Measurements of the dynamical cooling rate associated with the vertical transport of heat by dissipating gravity waves in the mesopause region at the Starfire Optical Range, New Mexico, Journal of Geophysical Research: Atmospheres, 103, 16909–16926, 10.1029/98jd00683, 1998.

Geller, M. A. and Gong, J.: Gravity wave kinetic, potential, and vertical fluctuation energies as indicators of different frequency gravity waves, Journal of Geophysical Research: Atmospheres, 115, 10.1029/2009jd012266, 2010.

Guarino, M. V., Gardner, C. S., Feng, W., Funke, B., García-Comas, M., López-Puertas, M., Kupilas, M. M., Marsh, D. R., and Plane, J. M. C.: A novel gravity wave transport parametrization for global chemistry climate models: description and validation, Journal of Advances in Modeling Earth Systems, 16, 10.1029/2023ms003938, 2024.

Guo, Y. and Liu, A. Z.: Seasonal variation of vertical heat and energy fluxes due to dissipating gravity waves in the mesopause region over the Andes, Journal of Geophysical Research: Atmospheres, 126, 10.1029/2020jd033825, 2021.

Hines, C. O.: Internal atmospheric gravity waves at ionospheric heights, Canadian Journal of Physics, 38, 1441–1481, 10.1139/p60-150, 1960.

Holton, J. R.: The influence of gravity wave breaking on the general circulation of the middle atmosphere, Journal of the Atmospheric Sciences, 40, 2497–2507, 10.1175/1520-0469(1983)040<2497:Tiogwb>2.0.Co;2, 1983.

Li, Q., Xu, J., Liu, H., Liu, X., and Yuan, W.: How do gravity waves triggered by a typhoon propagate from the troposphere to the upper atmosphere?, Atmospheric Chemistry and Physics, 22, 12077–12091, 10.5194/acp-22-12077-2022, 2022.

Li, T., She, C. Y., Liu, H. L., and Montgomery, M. T.: Evidence of a gravity wave breaking event and the estimation of the wave characteristics from sodium lidar observation over Fort Collins, CO (41°N, 105°W), Geophysical Research Letters, 34, 10.1029/2006gl028988, 2007.

Li, T., Ban, C., Fang, X., Li, F., Cen, Y., Lai, D., Sun, C., Sun, L., Zhang, J., and Xu, C.: Seasonal variation in gravity wave momentum and heat fluxes in the mesopause region observed by sodium lidar, Journal of Geophysical Research: Atmospheres, 127, 10.1029/2022jd037558, 2022.

Lindzen, R. S.: Turbulence and stress owing to gravity wave and tidal breakdown, Journal of Geophysical Research: Oceans, 86, 1981.

Liu, A. Z.: Estimate eddy diffusion coefficients from gravity wave vertical momentum and heat fluxes, Geophysical Research Letters, 36, 10.1029/2009gl037495, 2009.

Liu, H. L.: Temperature changes due to gravity wave saturation, Journal of Geophysical Research: Atmospheres, 105, 12329–12336, 2000.

Liu, H. L.: Effective vertical diffusion by atmospheric gravity waves, Geophysical Research Letters, 48, 10.1029/2020gl091474, 2021.

Liu, H. L., Hays, P. B., and Roble, R. G.: A numerical study of gravity wave breaking and impacts on turbulence and mean state, Journal of the Atmospheric Sciences, 56, 2152–2177, 10.1175/1520-0469(1999)056<2152:ANSOGW>2.0.CO;2, 1999.

Liu, H. L., Lauritzen, P. H., Vitt, F., and Goldhaber, S.: Assessment of Gravity Waves From Tropopause to Thermosphere and Ionosphere in High-Resolution WACCM-X Simulations, Journal of Advances in Modeling Earth Systems, 16, 10.1029/2023ms004024, 2024.

Liu, H. L., McInerney, J. M., Santos, S., Lauritzen, P. H., Taylor, M. A., and Pedatella, N. M.: Gravity waves simulated by high-resolution Whole Atmosphere Community Climate Model, Geophysical Research Letters, 41, 9106–9112, 10.1002/2014gl062468, 2014.

Liu, H. L., Bardeen, C. G., Foster, B. T., Lauritzen, P., Liu, J., Lu, G., Marsh, D. R., Maute, A., McInerney, J. M., Pedatella, N. M., Qian, L., Richmond, A. D., Roble, R. G., Solomon, S. C., Vitt, F. M., and Wang, W.: Development and validation of the Whole Atmosphere Community Climate Model with thermosphere and ionosphere extension (WACCM-X 2.0), Journal of Advances in Modeling Earth Systems, 10, 381–402, 10.1002/2017ms001232, 2018.

Liu, X., Xu, J., Yue, J., and Liu, H.: Gravity-wave-perturbed wind shears derived from SABER temperature observations, Atmospheric Chemistry and Physics, 20, 14437–14456, 10.5194/acp-20-14437-2020, 2020.

Liu, X., Xu, J., Yue, J., and Vadas, S. L.: Numerical modeling study of the momentum deposition of small amplitude gravity waves in the thermosphere, Annales Geophysicae, 31, 1–14, 10.5194/angeo-31-1-2013, 2013.

Liu, X., Xu, J., Yue, J., Yuan, T., She, C. Y., and Vital, L. F. R.: Assessments the Long-Term Stability of the SABER Temperature Measurement in the Middle Latitude MLT Region, Journal of Geophysical Research: Space Physics, 131, 10.1029/2025ja034476, 2026.

Liu, X., Yue, J., Xu, J., Wang, L., Yuan, W., Russell, J. M., and Hervig, M. E.: Gravity wave variations in the polar stratosphere and mesosphere from SOFIE/AIM temperature observations, Journal of Geophysical Research: Atmospheres, 119, 7368–7381, 10.1002/2013jd021439, 2014.

Liu, X., Yue, J., Xu, J., Garcia, R. R., Russell, J. M., Mlynczak, M., Wu, D. L., and Nakamura, T.: Variations of global gravity waves derived from 14 years of SABER temperature observations, Journal of Geophysical Research: Atmospheres, 122, 6231–6249, 10.1002/2017jd026604, 2017.

Lu, X., Chu, X., Li, H., Chen, C., Smith, J. A., and Vadas, S. L.: Statistical characterization of high-to-medium frequency mesoscale gravity waves by lidar-measured vertical winds and temperatures in the MLT, Journal of Atmospheric and Solar-Terrestrial Physics, 162, 3–15, 10.1016/j.jastp.2016.10.009, 2017.

Malavart, A., Hoffmann, A., Bräuer, F., Hofmann, J., Hélière, A., Carnicero Dominguez, B., Friedl-Vallon, F., Sinnhuber, B.-M., Preusse, P., Walker, K., Riel, S., Keim, C., Schweikle, S., Nikolov, S., Belloc, C., St-Amand, C., Loew, H., Krisch, I., Sandri, P., Moser, K., Klimaszewski, M., Posselt, W., Giaccari, P., Caullier, F., and Abdon, S.: EE-11 candidate mission CAIRT: an overview of the Phase 0 and A System studies, Environmental Remote Sensing, SPIE2025.

Mlynczak, M. G. and Solomon, S.: A detailed evaluation of the heating efficiency in the middle atmosphere, Journal of Geophysical Research: Atmospheres, 98, 10517–10541, https://doi.org/10.1029/93JD00315, 1993.

https://doi.org/10.5194/egusphere-2026-5223
Preprint. Discussion started: 9 September 2026

Mlynczak, M. G., Hunt, L. A., Russell, J. M., and Marshall, B. T.: Updated SABER Night Atomic Oxygen and Implications for SABER Ozone and Atomic Hydrogen, Geophysical Research Letters, 45, 5735–5741, 10.1029/2018gl077377, 2018.

Mlynczak, M. G., Hunt, L. A., Garcia, R., Lopez-Puertas, M., Mertens, C. J., Nowak, N., and Marshall, B. T.: Energy Conservation in the Cooling and Contracting Upper Mesosphere and Lower Thermosphere, Geophysical Research Letters, 51, 10.1029/2024gl109757, 2024.

Mlynczak, M. G., Hunt, L. A., Garcia, R. R., Harvey, V. L., Marshall, B. T., Yue, J., Mertens, C. J., and Russell, J. M.: Cooling and Contraction of the Mesosphere and Lower Thermosphere From 2002 to 2021, Journal of Geophysical Research: Atmospheres, 127, 10.1029/2022jd036767, 2022.

Mlynczak, M. G., Marshall, B. T., Garcia, R. R., Hunt, L., Yue, J., Harvey, V. L., Lopez-Puertas, M., Mertens, C., and Russell, J.: Algorithm Stability and the Long-Term Geospace Data Record From TIMED/SABER, Geophysical Research Letters, 50, 10.1029/2022gl102398, 2023.

Mlynczak, M. G., Daniels, T., Hunt, L. A., Yue, J., Marshall, B. T., Russell, J. M., Remsberg, E. E., Tansock, J., Esplin, R., Jensen, M., Shumway, A., Gordley, L., and Yee, J. H.: Radiometric Stability of the SABER Instrument, Earth and Space Science, 7, 10.1029/2019ea001011, 2020.

Ortland, D. A. and Alexander, M. J.: Gravity wave influence on the global structure of the diurnal tide in the mesosphere and lower thermosphere, Journal of Geophysical Research: Space Physics, 111, 10.1029/2005ja011467, 2006.

Remsberg, E. E., Marshall, B. T., Garcia-Comas, M., Krueger, D., Lingenfelser, G. S., Martin-Torres, J., Mlynczak, M. G., Russell, J. M., Smith, A. K., Zhao, Y., Brown, C., Gordley, L. L., Lopez-Gonzalez, M. J., Lopez-Puertas, M., She, C. Y., Taylor, M. J., and Thompson, R. E.: Assessment of the quality of the Version 1.07 temperature-versus-pressure profiles of the middle atmosphere from TIMED/SABER, Journal of Geophysical Research: Atmospheres, 113, 10.1029/2008jd010013, 2008.

Russell, J., Mlynczak, M. G., Gordley, L. L., Tansock, J., J. J., and Esplin, R. W.: Overview of the SABER experiment and preliminary calibration results, Proceedings Volume 3756, Optical Spectroscopic Techniques and Instrumentation for Atmospheric and Space Research III, 10.1117/12.366382, 1999.

Siskind, D. E., Eckermann, S. D., McCormack, J. P., Alexander, M. J., and Bacmeister, J. T.: Hemispheric differences in the temperature of the summertime stratosphere and mesosphere, Journal of Geophysical Research: Atmospheres, 108, 10.1029/2002jd002095, 2003.

Smith, A. K.: Physics and chemistry of the mesopause region, Journal of Atmospheric and Solar-Terrestrial Physics, 66, 839–857, 10.1016/j.jastp.2004.01.032, 2004.

Su, L., Collins, R. L., Krueger, D. A., and She, C.-Y.: Statistical Analysis of Sodium Doppler Wind–Temperature Lidar Measurements of Vertical Heat Flux, Journal of Atmospheric and Oceanic Technology, 25, 401–415, 10.1175/2007jtecha915.1, 2008.

Tao, X. and Gardner, C. S.: Heat flux observations in the mesopause region above Haleakala, Geophysical Research Letters, 22, 2829–2832, 1995.

Torrence, C. and Compo, G. P.: A Practical Guide to Wavelet Analysis, Bulletin of the American Meteorological Society, 79, 61–78, 10.1175/1520-0477(1998)079<0061:Apgtwa>2.0.Co;2, 1998.

Vadas, S. L.: Compressible f-plane solutions to body forces, heatings, and coolings, and application to the primary and secondary gravity waves generated by a deep convective plume, Journal of Geophysical Research: Space Physics, 118, 2377–2397, 10.1002/jgra.50163, 2013.

Vadas, S. L. and Fritts, D. C.: Thermospheric responses to gravity waves: Influences of increasing viscosity and thermal diffusivity, Journal of Geophysical Research: Atmospheres, 110, 10.1029/2004jd005574, 2005.

Vadas, S. L., Fritts, D. C., and Alexander, M. J.: Mechanism for the Generation of Secondary Waves in Wave Breaking Regions, Journal of the Atmospheric Sciences, 60, 194–214, 2003.

Vadas, S. L., Zhao, J., Chu, X., and Becker, E.: The Excitation of Secondary Gravity Waves From Local Body Forces: Theory and Observation, Journal of Geophysical Research: Atmospheres, 123, 9296–9325, 10.1029/2017jd027970, 2018.

Walterscheid, R. L.: Dynamical cooling induced by dissipating internal gravity waves, Geophysical Research Letters, 8, 1235–1238, 10.1029/GL008i012p01235, 1981.

https://doi.org/10.5194/egusphere-2026-5223
Preprint. Discussion started: 9 September 2026

Wang, L. and Alexander, M. J.: Global estimates of gravity wave parameters from GPS radio occultation temperature data, Journal of Geophysical Research: Atmospheres, 115, 10.1029/2010jd013860, 2010.

Weinstock, J.: Heat flux induced by gravity waves, Geophysical Research Letters, 10, 165–167, 10.1029/GL010i002p00165, 1983.

Wu, X., Zhu, Y., Smith, A. K., Kaufmann, M., Jiang, G., Liu, S., and Xu, J.: A new data set of nighttime chemical heating rates in the upper mesosphere and lower thermosphere derived from SCIAMACHY OH (9–6) emissions and SABER profiles, Atmospheric Chemistry and Physics, 26, 4669–4683, 10.5194/acp-26-4669-2026, 2026.

Xu, J., Smith, A. K., and Ma, R.: A numerical study of the effect of gravity-wave propagation on minor species distributions in the mesopause region, Journal of Geophysical Research: Atmospheres, 108, 10.1029/2001jd001570, 2003.

Xu, J., Liu, H. L., Yuan, W., Smith, A. K., Roble, R. G., Mertens, C. J., Russell, J. M., and Mlynczak, M. G.: Mesopause structure from Thermosphere, Ionosphere, Mesosphere, Energetics, and Dynamics (TIMED)/Sounding of the Atmosphere Using Broadband Emission Radiometry (SABER) observations, Journal of Geophysical Research: Atmospheres, 112, 10.1029/2006jd007711, 2007.

Xu, J., Smith, A. K., Liu, H. L., Yuan, W., Wu, Q., Jiang, G., Mlynczak, M. G., and Russell, J. M.: Estimation of the equivalent Rayleigh friction in mesosphere/lower thermosphere region from the migrating diurnal tides observed by TIMED, Journal of Geophysical Research: Atmospheres, 114, 10.1029/2009jd012209, 2009.

Xue, X. H., Liu, H. L., and Dou, X. K.: Parameterization of the inertial gravity waves and generation of the quasi-biennial oscillation, Journal of Geophysical Research: Atmospheres, 117, 10.1029/2011jd016778, 2012.

Yamashita, C., England, S. L., Immel, T. J., and Chang, L. C.: Gravity wave variations during elevated stratopause events using SABER observations, Journal of Geophysical Research: Atmospheres, 118, 5287–5303, 10.1002/jgrd.50474, 2013.

Yiğit, E. and Medvedev, A. S.: Heating and cooling of the thermosphere by internal gravity waves, Geophysical Research Letters, 36, 10.1029/2009gl038507, 2009.

Yue, J. and Wang, N.: Estimation of adiabatic cooling and warming in the mesosphere and lower thermosphere, Journal of Atmospheric and Solar-Terrestrial Physics, 269, 10.1016/j.jastp.2025.106492, 2025.